Theoretical and Applied Fracture Mechanics 127 (2023) 104005

Contents lists available at ScienceDirect

Theoretical and Applied Fracture Mechanics

journal homepage: www.elsevier.com/locate/tafmec

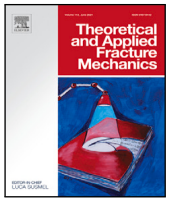

A robust identification procedure for phase field fracture mechanics parameters

Rakesh Kumar Tota [a,b,*], Marco Paggi [a]

[a] IMT School for Advanced Studies Lucca, Piazza San Francesco, 19, 55100, Lucca, Italy
[b] School of Marine Engineering and Technology, Indian Maritime University, Chennai, 600119, Tamil Nadu, India

ARTICLE INFO

Keywords:
Fracture mechanics
Phase field method
Particle swarm optimization
Parameters' identification
ABS co-polymers

ABSTRACT

The classical Phase Field (PF) model for fracture mechanics of brittle materials based on the finite element method involves three parameters in addition to the Poisson ratio ν: the Young's modulus E, the fracture toughness G_c, and the internal length scale l_c. The latter is mathematically conceived as a numerical regularization parameter that should tend to zero to recover linear elastic fracture mechanics (LEFM) predictions. To address this issue, a robust algorithm is implemented in MATLAB, which combines Particle Swarm Optimization (PSO) and the Phase Field (PF) approach to fracture based on the finite element method. The algorithm has been applied to a series of uni-axial tensile tests (with E and l_c to be identified) and to three-point bending tests (with E, l_c and also G_c to be identified) on specimens made of ABS material. Results show that the optimal values of E and G_c are consistent in both tests, while l_c presents a significant dependency upon the test type. Therefore, different values of the internal length scale should be identified and used to match the experimental responses under uni-axial tension or bending.

1. Introduction

The phase field approach to fracture is an emerging computational technique for the simulation of complex crack paths in solids and structures.

The development of numerical methods within the Finite Element Analysis (FEA) to predict fracture onset, propagation, and branching in materials and structures has been the subject of intensive research since the 1970s. Those methods are requested to tackle technical problems that analytical methods cannot address. In this regard, the Cornell Fracture Group [1] developed FEA software based on linear elastic fracture mechanics (LEFM). These methods were based on inserting singular finite elements at the crack tip to approximate the singular stress field and compute the stress-intensity factors according to the displacement correlation technique or the J-integral method. Although efficient for 2D problems, the extension of the methodology to 3D geometries, also with multiple materials, is quite complex since the theoretical definition of the generalized stress-intensity factors and the implementation of the related computational procedures require a significant effort [2].

Alternatively, Continuum Damage Mechanics (CDM) models accounting for a smeared crack representation [3] can address both crack nucleation and propagation stages. To avoid mesh dependency of local damage formulations, integral-based nonlocal and gradient-enhanced procedures have been proposed [4–8]. Moreover, extended FE strategies with nodal kinematic enrichment (extended-FEM, X-FEM) that rely on Partition of Unity Methods (PUM) [9–11] and element enrichment formulations (enhanced-FEM, E-FEM) [12–15] have also seen a considerable development. These methods present limitations for the simulation of complex failure modes that require predicting crack initiation, propagation, branching, and coalescence from multiple points.

In this regard, the phase field (PF) approach to fracture proposed in [16] based on $\Gamma-$convergence [17] presents several advantages. The above approach incorporates a non-local formulation that can retrieve the classical energy-based Griffith criterion [18] as a limit case when the internal length scale of the model tends to zero. Significant progress has been made regarding the numerical implementation of the phase field approach to fracture in FEA codes, see e.g. [19–21]. Some recent work on the phase field for fracture and its application can be found in [22–24]. This methodology appears to be very promising in reproducing not only the limit case of LEFM but also diffuse damage scenarios depending on the choice of the model parameters. It has been tested in relation to real experiments on brittle PMMA samples with notches and holes in [25]. Results have shown that the phase field approach to fracture can closely reproduce the experimental results not only in

* Corresponding author at: IMT School for Advanced Studies Lucca, Piazza San Francesco, 19, 55100, Lucca, Italy.
E-mail addresses: totarakesh.kumar@imtlucca.it, totarakeshk@imu.ac.in (R.K. Tota).

https://doi.org/10.1016/j.tafmec.2023.104005
Received 6 May 2023; Received in revised form 6 July 2023; Accepted 10 July 2023
Available online 13 July 2023

Nomenclature

Acronyms

2D	Two dimensional space
3D	Three dimensional space
ABS	Acrylonitrile butadiene styrene
FEA	Finite element analysis
FEM	Finite element method
PF	Phase field approach to fracture
PMMA	Poly(methyl methacrylate)
PSO	Particle swarm optimization
STD	Standard deviation

Variable notation

$\mathbf{u}$	Displacement field
ν	Poisson ratio
ϕ	Phase field variable
Y	PSO target cost function
E	Young's modulus
G_c	Fracture energy
l_c	Internal length scale parameter

terms of the crack pattern but also in terms of force–displacement and local stress measures. In [25], parameters' identification for each type of simulated test was conducted manually. Still, preliminary results showed significant concerns, especially for the popular AT2 phase field model [19,26] referred to as the standard Ambrosio-Tortorelli model in the applied mathematics community [27]. Specifically, the internal length scale of the phase field approach was a rather complex parameter to be identified.

The value of the peak traction in a simulated uni-axial tensile test is affected by the choice of the internal length scale of the phase field model. A possible correlation between material strength (σ_c) and the internal length scale (l_c) can be formally established, see [28], which has led to the wide belief that l_c estimated from uni-axial tensile tests can be consistently valid also for any other geometry and loading conditions. This belief has been questioned in [25], where manual identification of the internal length scale for all the conducted tests on PMMA samples with different geometry and loading conditions has shown that, especially for the AT2 model, it is not possible to use the value of the uni-axial tensile tests to reproduce all the experimental trends accurately. This motivates the need to develop a robust identification procedure to extract the optimal value of the internal length scale directly from experimental results. In the literature, [29] applied the Bayesian approach to estimate the phase field model's bulk and shear moduli, tensile strength, and fracture toughness to match the three-point bending test experimental result data. In the above work, to calculate the internal length scale parameter, an expression for the uni-axial case mentioned in [28] is used, and no information is provided on how to choose the internal length scale parameter for the phase field model if there is a change in geometry and loading conditions. Thus, an automatic identification procedure is required and can be applied to evaluate the internal length scale parameter of the phase field model directly from the experimental data for conditions different from the uni-axial tensile tests.

Therefore, in this work, we propose a robust material parameters' identification procedure for the phase field approach to fracture based on Particle Swarm Optimization (PSO). This heuristic approach has been demonstrated to be extremely robust in the case of mechanical problems involving multiple nonlinearities, as shown in [30], such as plasticity and cohesive fracture. Therefore it is considered an excellent candidate also for phase field diffuse damage. The article is structured as follows: in Section 2, the AT2 phase field approach is briefly outlined, highlighting the issue of parameters' identification. Section 3 focuses on the proposed model parameters' identification procedure in relation to a benchmark test related to PF fracture propagation. Section 4 discusses the application of the proposed methods to experimental data related to ABS specimens, showing how the algorithm can automatically identify the mean and the standard deviation of the phase field fracture parameters for uni-axial and three-point bending tests. ABS material has been selected for its importance in additive manufacturing and injection molding applications.

2. The phase field approach to fracture

Let us consider a linear elastic continuum domain $\Omega \subset \mathbb{R}^B$ in the reference configuration with dimension $B \in [1,3]$. A crack may nucleate and propagate from already-existing notches or stress-concentrated areas. This phenomenon causes a displacement field $\mathbf{u}$ in the body that may show a discontinuity in correspondence with the locally spreading fracture. In the phase field approach to fracture, the sharp displacement discontinuity will be smeared out by introducing a suitable nonlocal regularization which introduces an unknown scalar damage variable ϕ in the domain. The problem reduces in finding the displacement $\mathbf{u}$ and the phase field damage variable ϕ, subject to the equilibrium conditions of the solid body, the evolution equation for damage coupled with the mechanical field and the boundary conditions related to the specific model geometry.

The total potential energy functional of the continuum Ω proposed by Francfort–Marigo [16] with a prospective evolving crack surface Γ is given by

$$\Pi(\mathbf{u},\phi) = \underbrace{\int_\Omega \Psi_E(\boldsymbol{\varepsilon}(\boldsymbol{u}),\phi)\,\mathrm{d}\Omega}_{\text{internal elastic energy}} + \underbrace{\int_\Omega \Psi_S(\phi)\,\mathrm{d}\Omega}_{\text{energy due to crack propagation}} \underbrace{- \int_\Omega \mathbf{b}\mathbf{u}\,\mathrm{d}\Omega - \int_{\partial\Omega_t} \bar{\mathbf{t}}\mathbf{u}\,\mathrm{d}\partial\Omega}_{\text{external loads}} \tag{1}$$

in which $\mathbf{b}$ and $\bar{\mathbf{t}}$ are body forces and boundary tractions, respectively. $\Psi_E(\boldsymbol{\varepsilon},\phi)$ is the internal energy density function [20] defined as

$$\Psi_E(\boldsymbol{\varepsilon},\phi) = g(\phi)\Psi_0^+(\boldsymbol{\varepsilon}) + \Psi_0^-(\boldsymbol{\varepsilon}) \tag{2}$$

where $g(\phi) = (1-\phi)^2 + \kappa_p$ is the stress degradation function dependent upon the phase field damage variable ϕ, κ_p a small number to avoid ill-conditioning of the stiffness matrix for $\phi \to 1$. Ψ_0^+ and Ψ_0^- are the tensile and compressive energies, respectively. Damaging the elastic energy of the material takes place only in case of tensile stress states [31].

In the framework of the phase field regularization [32], the fracture energy contribution $\Psi_S(\phi)$ is smeared over the domain. The surface integral (in 3D) or the line integral (in 2D) over Γ is therefore approximated with an integral over the domain Ω:

$$\int_\Omega \Psi_S(\phi) := \int_\Gamma G_c\,\mathrm{d}\Gamma \approx \int_\Omega G_c\gamma\,\mathrm{d}\Omega \approx \frac{G_c}{2}\int_\Omega \left[l_c\nabla\phi\cdot\nabla\phi + \frac{\phi^2}{l_c}\right]\mathrm{d}\Omega \tag{3}$$

where G_c is the fracture energy and l_c is the internal length scale parameter of the phase field.

The total energy functional therefore reads:

$$\Pi = \int_\Omega (g(\phi)\Psi_0^+(\boldsymbol{\varepsilon}) + \Psi_0^-(\boldsymbol{\varepsilon}))\,\mathrm{d}\Omega + \int_\Omega \frac{G_c}{2}\left[l_c\nabla\phi\cdot\nabla\phi + \frac{1}{l_c}\phi^2\right]\mathrm{d}\Omega - \int_\Omega \mathbf{b}\mathbf{u}\,\mathrm{d}\Omega - \int_{\partial\Omega_t}\bar{\mathbf{t}}\mathbf{u}\,\mathrm{d}\partial\Omega_t \tag{4}$$

The weak form of the problem is determined through the minimization of the above functional, which is done by computing its virtual variation with respect to the primary independent field variables:

$$\delta\Pi = \frac{\partial\Pi}{\partial\mathbf{u}}\delta\mathbf{u} + \frac{\partial\Pi}{\partial\phi}\delta\phi \tag{5}$$

which yields:

$$\delta\Pi = \int_\Omega \sigma\delta\varepsilon \mathrm{d}\Omega - \int_\Omega 2(1-\phi)\delta\phi\Psi_0^+(\boldsymbol{\varepsilon})\,\mathrm{d}\Omega + \int_\Omega G_c\left(l_c\nabla\phi\nabla\delta\phi + \frac{1}{l_c}\phi\delta\phi\right)\mathrm{d}\Omega - \int_\Omega b\delta u\,\mathrm{d}\Omega - \int_{\partial\Omega_t}\bar{t}\delta u\,\mathrm{d}\partial\Omega_t \tag{6}$$

In addition to the above, an irreversibility condition upon ϕ has to be introduced to avoid healing of the material during damage evolution. Again, we follow here the approach in [20], which introduces the following history variable $\mathcal{H}$ in Eq. (6).

$$\mathcal{H} = \begin{cases} \Psi_0^+(\boldsymbol{\varepsilon}) & \text{if } \Psi_0^+(\boldsymbol{\varepsilon}) > \mathcal{H}_n \\ \mathcal{H}_n & \text{otherwise} \end{cases} \tag{7}$$

where $\mathcal{H}_n$ is the value of Ψ_0^+ at the previous pseudo-time step of a quasi-static simulation with pseudo-time increasing applied displacements/loads. Note that the function $\mathcal{H}$ satisfies the Karush-Kuhn–Tucker conditions:

$$\Psi_0^+ - \mathcal{H} \le 0,\ \dot{\mathcal{H}} \ge 0,\ \dot{\mathcal{H}}\left(\Psi_0^+ - \mathcal{H}\right) = 0 \tag{8}$$

The strong form associated with the weak form in Eq. (6) is:

$$\nabla\cdot\sigma + \mathbf{b} = 0 \text{ in } \Omega, \quad \sigma\cdot n = \bar{t} \text{ on } \partial\Omega_{\bar{t}}, \quad u = \bar{u} \text{ on } \partial\Omega_u \tag{9}$$

$$-G_c l_c\nabla^2\phi + \left[\frac{G_c}{l_c} + 2\Psi(\boldsymbol{\varepsilon})\right]\phi = 2\Psi(\boldsymbol{\varepsilon}) \text{ in } \Omega, \quad \nabla\phi\cdot n = 0 \text{ on } \partial\Omega \tag{10}$$

To solve the above weak form, the finite element discretization is introduced by projecting $\delta\Pi$ onto a suitable functional space. Usually, a functional space composed of linear or quadratic polynomials is a natural choice. However, other spaces like those defined by NURBS could be exploited [33], and it is a current research direction. Moreover, in the case of polynomials, $h-$, $p-$, and $hp-$refining schemes are currently investigated to improve the efficiency of the computational method.

Therefore, the finite element implementation of the PF approach using the staggered solution scheme method [20] is implemented to find the displacement field and the phase field variable.

3. The proposed parameters' identification procedure and benchmark tests

The issue of model parameters' identification for the phase field approach to fracture is relevant for technical applications, as outlined in the introduction. In this direction, evolution-based Genetic algorithms (GA) [34]; swarm intelligent-based particle swarm optimization (PSO) algorithm [35]; teaching and learning based algorithm (TLBO) [36], and JAYA algorithm [37] are some of the well-known popular algorithms in the literature which proved to be efficient for non-linear constrained and unconstrained problems. The above algorithms have their advantages and disadvantages depending on the application. Moreover, a hybrid algorithm considering a combination of the above algorithms could be more efficient than each one separately. The aim of the present work is not to compare all the possible algorithms but rather to propose and assess the performance of a heuristic optimization technique (PSO in particular) for the present inverse problem. PSO has been proven to be a very effective tool in model parameters' identification for nonlinear fracture mechanics problems involving plasticity and cohesive fracture [30]. Fine-tuning of the PSO algorithm parameters will overcome the performance of most of the algorithms, see e.g. [34,36,37].

PSO [35] allows the scattering of certain populations of particles in a pre-defined parametric design space. PSO particles are then optimized by achieving a minimum target cost function (Υ) to match the user desired mechanical response. In the present problem, the Young's modulus (E), fracture toughness (G_c), and the phase field internal length scale parameter (l_c) are the parameters defining each swarm particle position. Considering a force–displacement mechanical response (from experiments or desired), the target cost function (Υ) for every swarm particle is defined as

$$\Upsilon(\chi) = \sqrt{\sum_{d=1}^{N}\left[\frac{\Delta F_d(\chi)}{\hat{F}_d(\chi)}\right]^2} \tag{11}$$

where $\Delta F_d(\chi) = F_d - \hat{F}_d(\chi)$, in which F_d denotes the history of simulated forces for the range of imposed pseudo-time steps d ($d = 1, \ldots, N$). The simulated test is conducted under displacement control till 'N' number of imposed displacements for a given set of trial model parameters. Analogously, $\hat{F}_d(\chi)$ represents the target values of forces for the same 'N' imposed displacements. The PSO algorithm is detailed in Algorithm 1 in relation to the methodology outlined in Appendix.

Algorithm 1 Particle swarm optimization

Input data : number of swarm particles $\mathrm{N_p}$, maximum number of iterations $\mathrm{It_{max}}$, PSO algorithm parameters $\mathbf{W_i}, \mathbf{C_c}, \mathbf{S_c}, \mathrm{w_{damp}}$
Output data : optimized particle solutions $\mathbf{P_g}$ for minimum cost function Υ
———**Initialization**———
for all $i = 1 : \mathrm{N_p}$ **do**
  Generate a population of swarm particles with random particle position $\chi_\mathbf{i}^\mathbf{0}$ in three dimensional ($\wp = 3$) parametric space (E, G_c, l_c) variables under constrained solution search space for example as defined in Eq. (12)
  Evaluate cost function $\Upsilon(\chi_\mathbf{i}^\mathbf{0})$
  Assign local best swarm particle position vector $\mathbf{P_i^0} \leftarrow \chi_\mathbf{i}^\mathbf{0}$
  Assign zero swarm particle velocity vector $\bigvee_i^\mathbf{0}$
end for
Assign $\mathbf{P_g^0} \leftarrow \underset{\chi_i^0}{\mathrm{argmin}}\Upsilon(\chi_\mathbf{i}^\mathbf{0})$
Assign particle velocity range $\mathrm{V_r} = [\mathrm{v_{min}},\ \mathrm{v_{max}}]$
———**Main loop of PSO algorithm**———
for $k = 1 : \mathrm{It_{max}}$ **do**
  for all $i = 1 : \mathrm{N_p}$ **do**
    Update particle velocity vector $\bigvee_i^\mathbf{k}$ from Eq. (A.1)
    check $\bigvee_i^\mathbf{k}$ in limits of $\mathrm{V_r}$, if not reassign $\bigvee_i^\mathbf{k}$ in range $\mathrm{V_r}$
    Update particle position vector $\chi_\mathbf{i}^\mathbf{k}$ from Eq. (A.2)
    if $\chi_\mathbf{i}^\mathbf{k} \notin \wp$ **then**
      reassign randomly $\chi_\mathbf{i}^\mathbf{k}$ *in* $\wp$
    end if
    if $\Upsilon(\chi_\mathbf{i}^\mathbf{k}) < \Upsilon(\mathbf{P_i^{k-1}})$ **then**
      Update local best particle position $\mathbf{P_i^k}$ from Eq. (A.3)
      if $\Upsilon(\mathbf{P_i^k}) < \Upsilon(\mathbf{P_g^{k-1}})$ **then**
        Update global best particle position $\mathbf{P_g^k}$ from Eq. (A.4)
      end if
    end if
  end for
  $\mathbf{W_i} \leftarrow \mathbf{W_i} \times \mathrm{w_{damp}}$
end for

As a benchmark test, to show the applicability of PSO to parameters identification of phase-field fracture models, we consider here a Mode I single edge notch test (see Fig. 1). The following properties are set as an input for the simulation ($E = 210$ GPa, $G_c = 2.7$ kN/mm, $l_c = 0.1$ mm). The finite element discretization consists of 1949 four-noded bilinear quadrilateral finite elements with a minimum mesh size of 0.05 mm along the potential crack path.

The force–displacement curve predicted by phase field simulation is taken as the target function $\hat{F}_d$. This should be subsequently matched by the PSO algorithm applied to identify the material parameters that are considered to be unknown.

In this regard, we attempt to identify all three material parameters simultaneously. In the 3D parameter space, we consider $N_p = 30$

Table 1
Set of input data to generate target responses and range of parameters for the robustness test. The last column reports the error of the identified parameters concerning the values used in the input.

Case	G_c (kN/mm)	l_c (mm)	Range E (GPa)	Range G_c (kN/mm)	Range l_c (mm)	Absolute error % {E, G_c, l_c}
1	2.7	0.3	180–230	1.2–3.8	0.02–0.45	{0.078, 0.10, 0.037}
2	2.7	0.5	180–230	1.2–3.8	0.02–0.70	{0.116, 0.07, 0.018}
3	2.7	0.7	180–230	1.2–3.8	0.02–0.90	{0.312, 0.11, 0.048}
4	4.0	0.1	180–230	1.2–5.5	0.02–0.20	{0.297, 0.38, 0.032}
5	6.5	0.1	180–230	1.2–8.0	0.02–0.20	{0.078, 0.28, 0.015}
6	8.0	0.1	180–230	1.2–10.0	0.02–0.20	{0.252, 0.28, 0.014}
7	4.0	0.1	180–230	1.2–5.5	0.02–0.20	{1.075, 1.49, 0.107}
8	4.0	0.1	180–230	1.2–5.5	0.02–0.20	{0.120, 0.14, 0.009}

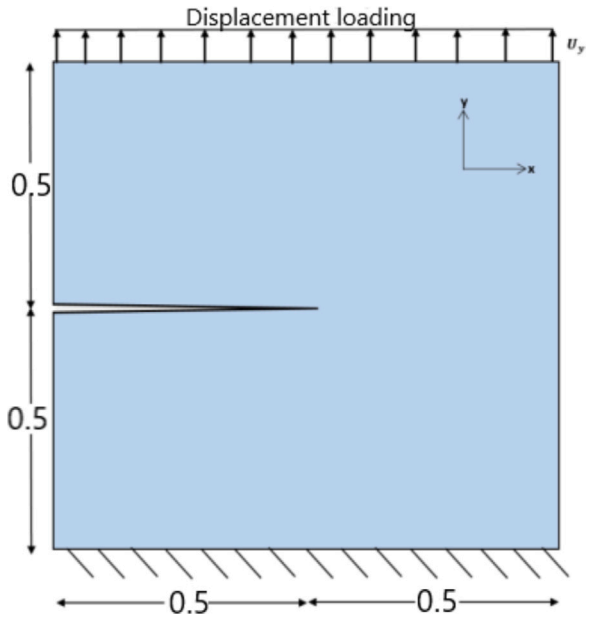

Fig. 1. Benchmark problem: geometry, loading and boundary conditions.

particles as population size, with a maximum of 150 iterations and the following PSO parameters: inertia weight $\mathbf{W_i} = 0.9$, damping weight $w_{damp} = 0.99$, cognitive coefficient $\mathbf{C_c} = 0.2$ and social coefficient $\mathbf{S_c} = 0.1$. The design-constrained particle space is defined as follows:

$$\mathscr{X} = \{180 < E < 230 \text{ GPa};\ 1.2 < G_c < 3.8 \text{ kN/mm};\ 0.02 < l_c < 0.2 \text{ mm}\} \tag{12}$$

which includes the values of the three parameters to be identified.

The evolution of swarm particles' position within the design space concerning PSO iterations are shown in Fig. 2. The identified values of the model parameters were $E = 209.967$ GPa, $G_c = 2.699$ kN/mm, $l_c = 0.099$ mm, which are very close to the parameters used to generate the target response numerically.

The cost function vs. a number of iterations is shown in Fig. 3, with an error in the force–displacement curve at the 54th iteration lower than 1×10^{-4}.

For completeness, the force–displacement curve corresponding to the identified model parameters accurately matches the target one, see Fig. 4.

The robustness of the PSO algorithm is also assessed by considering six different cases with parameters spanning over the G_c and l_c space for a fixed value of $E = 210$ GPa, see Table 1. The exact geometry and loading condition are considered as in Fig. 1.

Initial and final particles' positions are shown in Fig. 5 for cases 1, 2, and 3 related to the different values of l_c and in Fig. 6 for cases 4, 5, and 6 related to the different values of G_c. Further, to assess the convergence of the PSO algorithm, the velocity of the constriction factor-based approach [38] is adopted for case 8 (see Eq. (13)). The positive weights are applied to certain force–displacement points to set a priority while determining the cost function (Υ). If no positive weights are applied, all points in the force–displacement curve are treated equally. In the above-mentioned approach to guarantee stability [39], φ was set as 4.1 and $\mathbf{C_c} = \mathbf{S_c} = 2.05$. The velocity of the swarm particles is computed according to the following equation:

$$\begin{aligned} \bigvee_i^{\mathbf{k}} &= \kappa \times \left(\bigvee_i^{\mathbf{k-1}} + \mathbf{C_c} \times \mathbf{r_1} \times (\mathbf{P_i^k} - \chi_\mathbf{i}^\mathbf{k}) + \mathbf{S_c} \times \mathbf{r_2} \times (\mathbf{P_g^k} - \chi_\mathbf{i}^\mathbf{k})\right) \\ \kappa &= \frac{2}{\left|2 - \varphi - \sqrt{\varphi^2 - 4\varphi}\right|}, \text{where } \varphi = \mathbf{C_c} + \mathbf{S_c}, \varphi > 4 \end{aligned} \tag{13}$$

where κ is a constriction factor and $\mathbf{r_1}, \mathbf{r_2}$ are random numbers between 0 and 1. The explanation of the remaining parameters is mentioned in Appendix.

The robustness of the PSO algorithm is further examined by comparing case 4 without weights, case 7 with weights, and case 8 with weights and including the constriction factor for velocity. Fig. 7 clearly shows better convergence of case 8 compared to cases 4 and 7. Therefore, in the sequel, the PSO algorithm with the parameters used for case 8 is applied to identify fracture mechanics parameters concerning the experimental results of ABS material discussed in Section 4.

Finally, the PSO algorithm is compared with the TLBO algorithm to assess its robustness. For investigation, the benchmark problem shown in Fig. 1 is chosen, and the initial particle positions are the same and fixed for both PSO and TLBO algorithms (see Fig. 8(a)). For the PSO algorithm, case 8 is implemented. For the TLBO algorithm, the reader is referred to [36]. The algorithm design variables and their range is chosen as in case 8 (see Table 1) for both PSO and TLBO methods. The PSO algorithm identifies the optimal particles solution with ($E = 210.024$ GPa, $G_c = 4.0058$ kN/mm, and $l_c = 0.1004$ mm), which almost coincides with the output solution (see Fig. 8(b)). The TLBO algorithm identifies $E = 198.086$ GPa, $G_c = 3.6392$ kN/mm, and $l_c = 0.0778$ mm, which is not converging to the output solution (see Fig. 8(c)). Therefore, it can be inferred that the PSO algorithm performed better than the TLBO algorithm for the parameter identification of the present non-linear problem. Moreover, the computation time of TLBO is roughly twice that of PSO, since FEA for PF simulation of each particle is computed two times in the main TLBO algorithm loop.

4. Identification of material properties from experimental data of ABS co-polymers

The robustness of the PSO algorithm applied to the identification of fracture mechanics parameters is herein assessed in relation to experimental results of ABS co-polymer material subjected to tensile and three-point bending loading conditions.

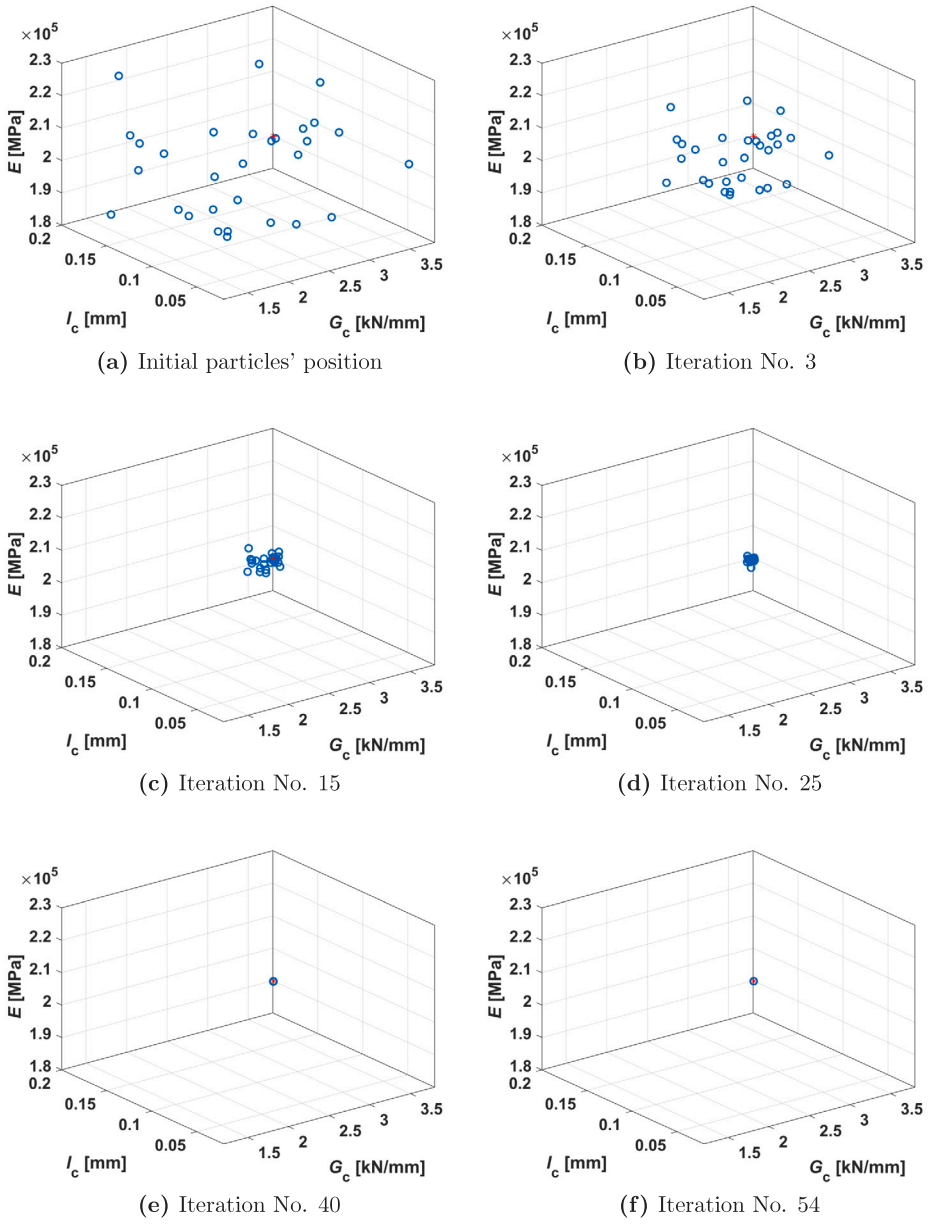

(a) Initial particles' position (b) Iteration No. 3

(c) Iteration No. 15 (d) Iteration No. 25

(e) Iteration No. 40 (f) Iteration No. 54

Fig. 2. Scatter representation of particles in the iterations of the PSO algorithm for the benchmark test problem.

A series of uni-axial and three-point bending experimental tests were carried out using the universal testing machine Zwick/Roell Z010TH available in the experimental laboratory of the Multi-scale Analysis of Materials Research Unit at IMT Lucca. The scatter in the experimental curves shown in Figs. 10(a) and 12(a) is due to the typical effect induced by a slight variation in the amount of additives used to reduce swelling of ABS materials for injection moulding [40].

The PF formulation based on the AT2 model has been applied to simulate the corresponding tests, and coupled with the PSO algorithm, parameter identification has been performed. All the routines are coded in MATLAB, release 2020b.

Young's modulus E, fracture parameters G_c (fracture energy), and l_c (internal length scale) were chosen as PSO swarm particle parameters to be identified. The range of ABS properties to conduct PSO-PF simulations were taken from literature: tensile strength $\sigma_{\max} \in \{22, 49\}$ MPa, $E \in \{1100, 2900\}$ MPa, Poisson's ratio $\nu = 0.37$ and fracture toughness $K_{I,c} \in \{1.2, 4.2\}\,\text{MPa}\sqrt{m}$. Exploiting the correlations $G_c = \frac{K_{I,c}^2(1-\nu^2)}{E}$ and $l_c = \frac{27}{256}\frac{G_c E}{(1-\nu^2)\sigma_{\max}^2}$, we derived the following range of variability for $G_c \in \{1.25, 13.8\}$ N/mm and $l_c \in \{0.25, 3.8\}$ mm.

4.1. Uni-axial tensile tests

Experimental tests were conducted and repeated 15 times on specimens of ABS material under uni-axial tensile loading conditions. The specimen geometry is length × width × thickness = 114 × 10.2 × 4.5 mm. The boundary conditions are depicted in Fig. 9. Stress–strain curves are shown in Fig. 10(a).

PF numerical simulations have been performed by replicating the experimental conditions (see Fig. 9). Dirichlet boundary condition $\phi =$

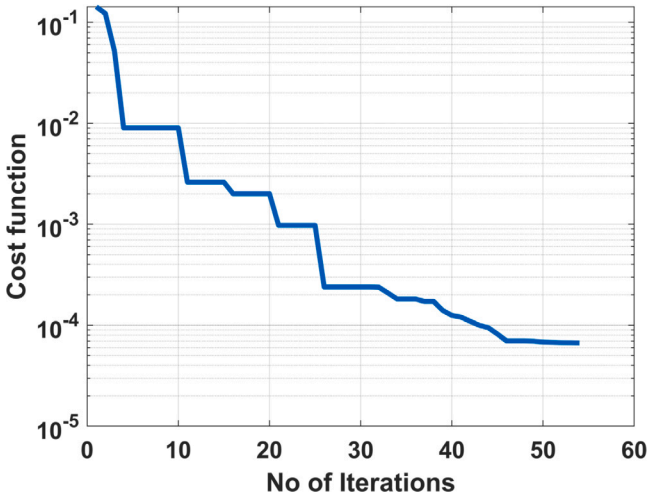

Fig. 3. Cost function vs. No. of PSO iterations for the benchmark test.

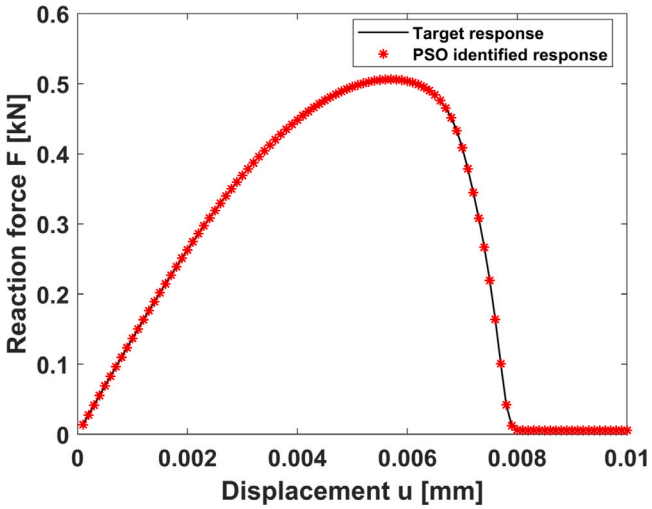

Fig. 4. Force–displacement curve and target curve.

0 [41,42] imposed on the phase field at both ends of the tensile test model.

Since uni-axial tensile tests are not suitable for fracture mechanics characterization, we set an average value of $G_C = 7.5$ N/mm from the literature for all 15 numerical simulations. E and l_c are the parameters to be identified that influence the initial linear elastic regime of the stress–strain curves and the material tensile strength (computed from the peak load value before specimen failure). Therefore, the PF-PSO simulations are conducted with swarm particles in the parameter space $(E,\ l_c)$, with admissible range for $E \in \{1100, 2900\}$ MPa and for $l_c \in \{0.25, 3.8\}$ mm. Fig. 10(b) shows the optimal PSO-PF response of the 15 stress–strain curves that minimize the error from the experimental ones. Table 2 collects the PSO-identified parameters for the 15 tests. From this analysis, considering the mean values and the standard deviations, the identified Young modulus corresponds to $\overline{E} \pm \sigma_E = 1157.904.01 \pm 34.8223$ MPa, and the internal length scale $\bar{l}_c \pm \sigma_{l_c} = 1.3361 \pm 0.0408$ mm.

Table 2
PSO identified E and l_c parameters for the 15 tests in Fig. 10, with their mean and standard deviation values.

Test #	E (MPa)	l_c (mm)
1	1130.39	1.281
2	1116.48	1.306
3	1215.08	1.415
4	1197.61	1.362
5	1183.24	1.320
6	1169.185	1.359
7	1120.50	1.290
8	1164.82	1.321
9	1123.67	1.273
10	1141.05	1.330
11	1107.73	1.392
12	1193.60	1.376
13	1152.43	1.318
14	1203.60	1.3472
15	1149.186	1.3508
Mean	1157.904	1.336
Std. dev.	34.8223	0.0408

4.2. Three-point bending tests

Three-point bending tests with notched samples are now considered since they can also be exploited for fracture mechanics characterization. Therefore, applying the PSO algorithm combined with the PF simulation framework is possible to identify all three model parameters, E, l_c, and G_c. Now these are critically compared with the outcome of the previous parameters' identification results concerning uni-axial tensile tests.

Experimental tests were conducted on a set of ABS specimens with an initial sharp V-notch under the three-point bending loading, see Fig. 11(a) and (b), showing the initially undeformed configuration and the specimen at failure. Fig. 11(b) shows the formation of crazing at the notch tip, which is highlighted by the change of color of ABS from yellow to white due to the stretching of the polymeric fibers during crack growth. The spread of crazing in the direction orthogonal to the mid-span cross-section is relatively consistent. It certainly represents a zone of diffuse damage that could be simulated using the phase-field approach to fracture with a finite -not vanishing- internal length scale l_c. Compared to PMMA investigated in [25], ABS is much less brittle.

The geometrical data are shown in Fig. 11(c). Fig. 11(d) depicts the FE mesh with linear quadrilateral finite elements with a fine discretization near the mid-cross-section and a coarser one far from the perspective crack path. A preliminary mesh sensitivity analysis has been performed for the PF simulations, considering 1614, 7076, or 13 984 finite elements using different degrees of refinement of the mesh far from the mid cross-section. The numerical predictions were almost unaffected by the resolution if the mid cross-section was properly discretized. The discretization in 1614 FE has been considered for the parameter identification issue to speed up computation time.

Force vs. mid-span displacement curves for the 15 tests are shown in Fig. 12. It compares the experimental curves (left panel) with the results of the numerical simulations (right panel) corresponding to the identified best model parameters by the PSO algorithm. Again, the following range of values has been considered $E \in \{1100, 2900\}$ MPa, $G_c \in \{1.25, 13.8\}$ N/mm, $l_c \in \{0.25, 3.8\}$ mm.

Table 3 collects all the identified parameters E, G_c, and l_c, with their respective mean values and standard deviations. Results can now be compared with the outcome of the identification performed on uni-axial tensile tests of the same materials, and that was limited to two model parameters, E and l_c. The identified Young modulus in the case of three-point bending tests was 1153.07 ± 35.03 MPa, and it is very close to the identified Young's modulus from the uni-axial tensile tests, which was estimated as 1157.90 ± 34.82 MPa. The identified fracture toughness from three-point bending tests is 8.85 ± 1.94 N/mm, and it compares

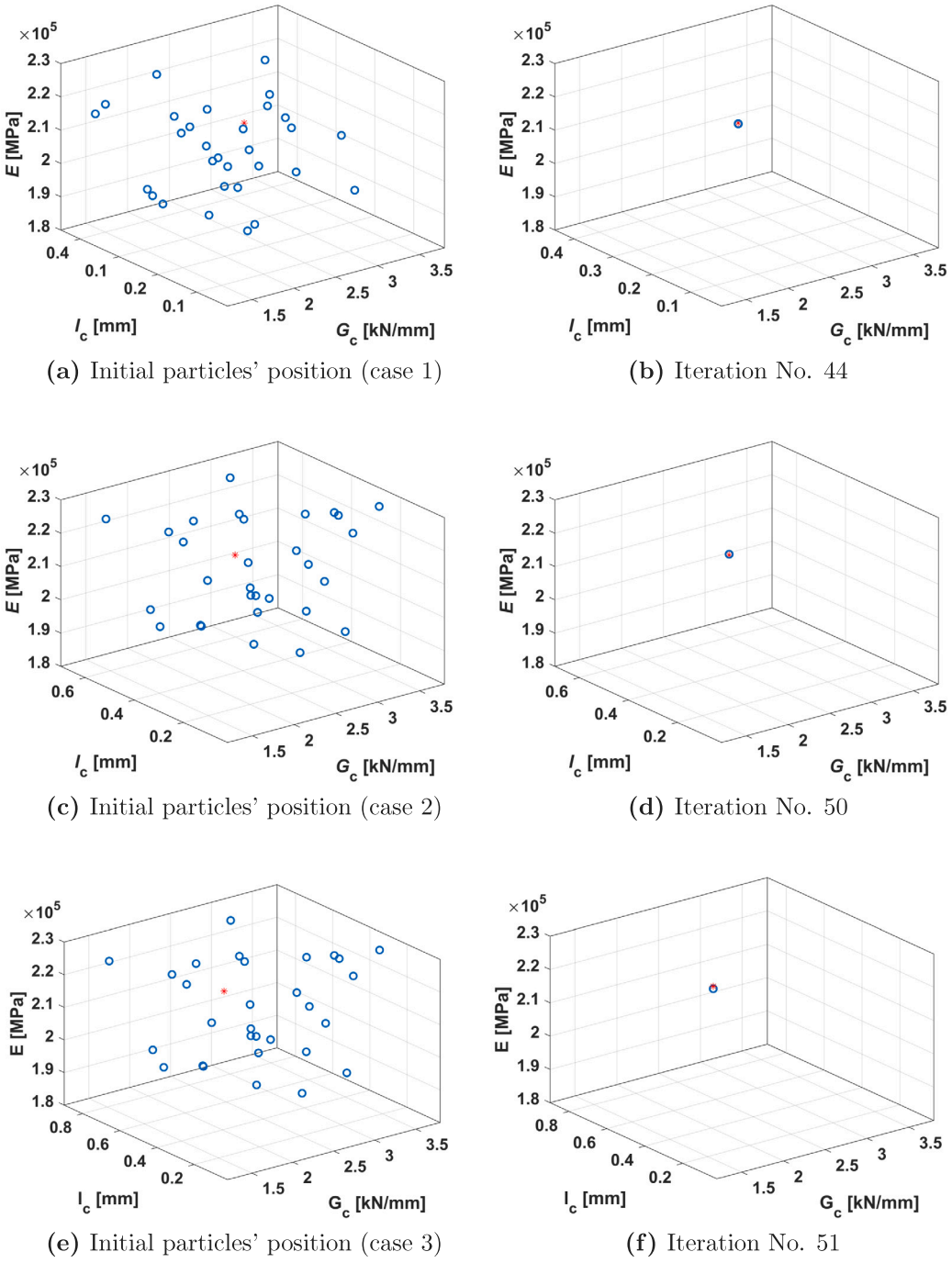

(a) Initial particles' position (case 1)

(b) Iteration No. 44

(c) Initial particles' position (case 2)

(d) Iteration No. 50

(e) Initial particles' position (case 3)

(f) Iteration No. 51

Fig. 5. Scatter representation of particles' position for cases 4, 5, and 6 whose parameters are collected in Table 1.

well with the average value taken from the literature and is equal to 7.5 N/mm that was set for all the uni-axial tensile tests. On the other hand, a significant discrepancy is observed as far as the internal length scale parameter l_c is concerned. The identified value from the three-point bending tests is 0.346 ± 0.157 mm, while from the uni-axial tensile tests it was 1.336 ± 0.041 mm. In addition to being smaller, the scatter also increased, as one can notice from the higher standard deviation value. Henceforth, inverse analysis procedure is strongly recommended to identify length scale parameters for different geometry loading test problems [43].

5. Conclusion

The critical issue of model parameters' identification for the phase field approach to fracture has been systematically addressed in this work. The proposed framework combines the heuristic identification approach based on Particle Swarm Optimization (PSO) and the FE implementation of the phase field (PF) approach to fracture, which has effectively identified model parameters. Both formulations have been implemented in MATLAB release 2020b in an ad hoc integrated FE software. Still, the methodology is general and requires a FE solver

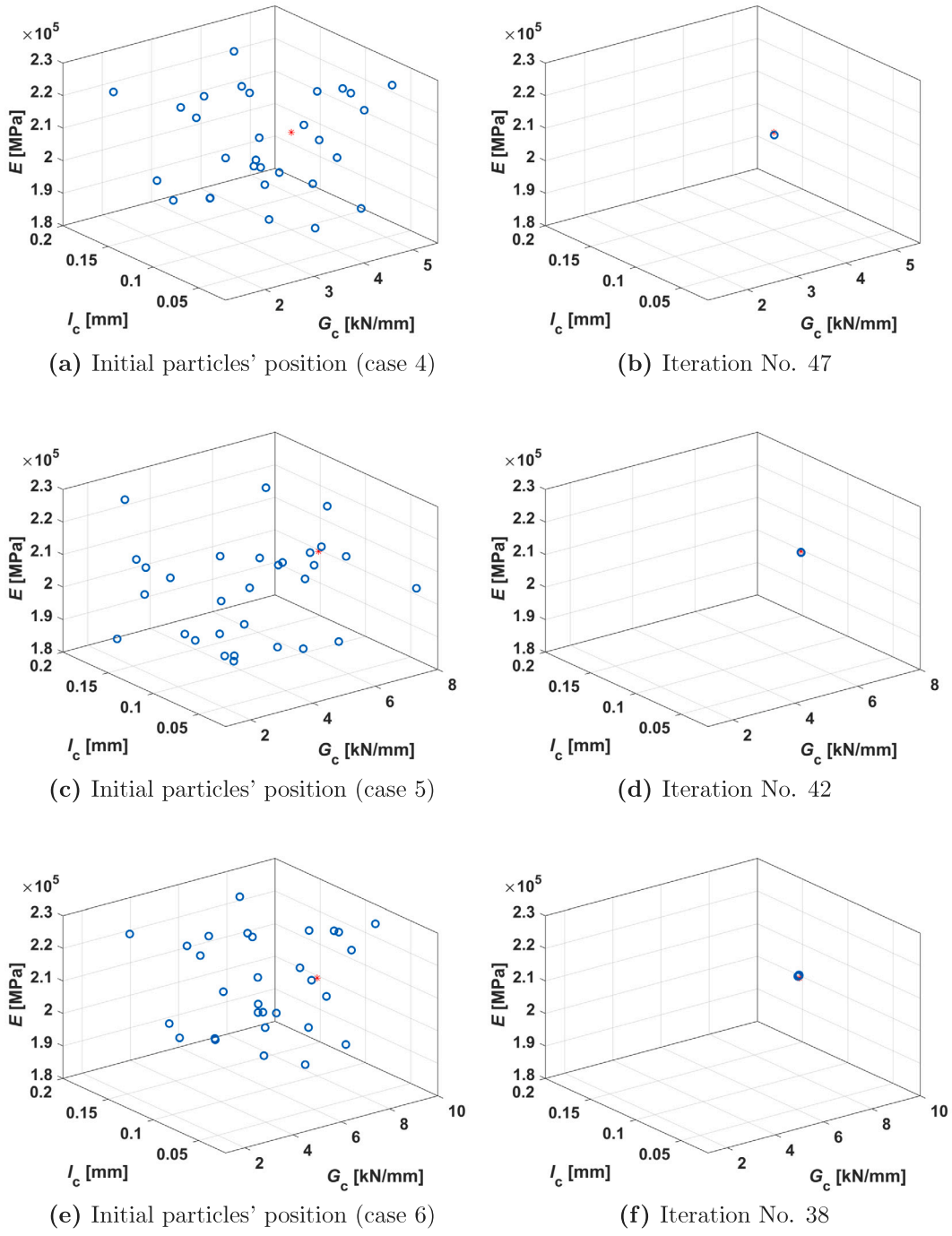

(a) Initial particles' position (case 4)

(b) Iteration No. 47

(c) Initial particles' position (case 5)

(d) Iteration No. 42

(e) Initial particles' position (case 6)

(f) Iteration No. 38

Fig. 6. Scatter representation of particles' position for cases 1, 2, and 3 whose parameters are collected in Table 1.

equipped with PF finite elements to be called by the PSO algorithm with a set of model parameters. The outcome of the FE simulation, in terms of the force–displacement curve, is again passed to the PSO algorithm, which computes the cost function and updates the particle coordinates, iterating the procedure till convergence. Therefore, any commercial FE software could be triggered using the system command called by the PSO algorithm.

The robustness of the proposed approach has been assessed in relation to a series of benchmark tests numerically generated in silico, i.e., by running a series of PF fracture simulations with known model parameters. The PSO algorithm could accurately retrieve the known input parameters from the identification procedure. In addition, the comparison of the results of the PSO algorithm with those of the TLBO algorithm shows that the PSO algorithm outperforms the TLBO algorithm.

The methodology has been finally applied to the critical problem of identifying the AT2 PF model parameters concerning real experimental tests on ABS materials which display a spread of diffuse damage typical

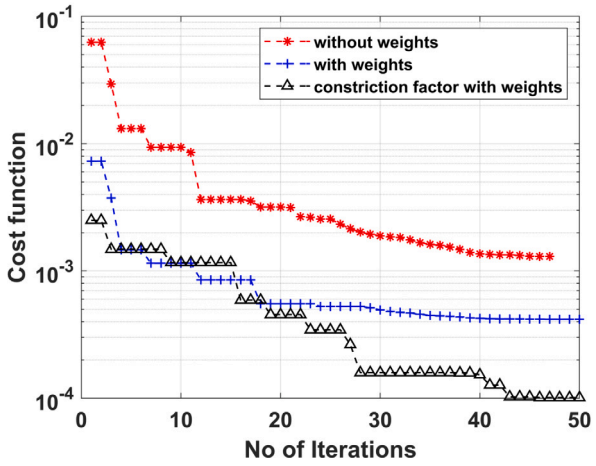

(a) Initial particles' position (case 6)

Fig. 7. Convergence study of the PSO algorithm for cases 4, 7, and 8, see Table 1.

Table 3
PSO identified E, G_c and l_c parameters for the 15 tests in Fig. 12, with their mean and standard deviation values.

Test #	E (MPa)	G_c (N/mm)	l_c (mm)
1	1189.39	7.56	0.250
2	1189.67	7.56	0.250
3	1101.17	8.83	0.256
4	1173.92	7.18	0.251
5	1176.29	7.84	0.250
6	1158.87	8.29	0.252
7	1179.82	7.38	0.290
8	1178.73	7.37	0.291
9	1133.36	8.35	0.303
10	1100.58	12.28	0.649
11	1100.40	12.21	0.639
12	1167.95	7.63	0.250
13	1139.86	10.23	0.369
14	1113.41	12.40	0.642
15	1192.62	7.62	0.256
Mean	1153.07	8.85	0.346
Std. dev. (STD)	35.03	1.94	0.157

of a quasi-brittle material. First, the PSO-PF combined approach has been applied to uni-axial tensile tests, identifying only E and l_c from the experimental curve up to the decay of the peak load. The uni-axial tests for this material cannot be used to assess the fracture energy, which has been set equal to the average value taken from the literature since the material undergoes strain localization with the crazing formation and large deformation in the post-peak branch, a situation far from fracture. The identification procedure has been repeated for sharp V-notched samples tested under three-point bending. This time, all the three model parameters (E, G_c, l_c) are identified since the post-peak branch can be reasonably well simulated as a result of a propagating crack.

The comparison between the identified parameters for the two test geometries shows that estimating l_c from uni-axial tensile tests and applying it to other testing geometries can lead to wrong predictions. To better highlight this result, we propose in Fig. 13 a comparison between PF simulations for the two types of tests conducted with different identified values of the internal length scale parameter: (*i*) identified values from uni-axial tests: $l_c = 1.37$ mm, $E = 1157.90$ MPa and $G_c = 7.5$ N/mm; (*ii*) identified values from notched three-point bending tests: $l_c = 0.35$ mm, $E = 1153.07$ MPa and $G_c = 8.85$ N/mm. The value of l_c affects both predictions in a significant manner. Therefore it is highly recommended to perform model parameters' identification for the AT2 PF model in relation to meaningful test geometries for fracture mechanics, not using uni-axial tensile tests to infer the value of phase field parameters.

To summarize the work, the proposed algorithm quantitively tracks the crack path phenomenon of the fracture problem. In addition, it also captures numerically experimental force–displacement curve responses by identifying phase field model parameters, which is a significant challenge due to the high dependence on the PF internal length scale parameter. Therefore PSO-PF numerically coupled algorithm provides a qualitative insight into the fracture design problems in avoiding under or overestimating critical structural limits of the load, which saves computational time and the cost of the material.

CRediT authorship contribution statement

Rakesh Kumar Tota: Methodology, Software, Validation, Formal analysis, Investigation, Data curation, Writing – original draft, Writing – review & editing, Visualization. **Marco Paggi:** Conceptualization, Methodology, Investigation, Writing – review & editing, Supervision.

Declaration of competing interest

The authors declare that they have no known competing financial interests or personal relationships that could have appeared to influence the work reported in this paper.

Data availability

Data will be used for subsequent research work.

Appendix. Particle swarm optimization algorithm

Particle swarm optimization (PSO) is applied to a continuous spatial domain where the cost function Y is minimized to converge swarm particles in the solution space region to the optimized position. Let us assume there are N_p swarm particle size population in a '$\wp$' dimensional parametric space domain. $\chi_{\mathbf{i}} := [\mathbf{x}_{i1}, \mathbf{x}_{i2}, \ldots, \mathbf{x}_{i\wp}]$, $\bigvee_{\mathbf{i}} := [\mathbf{v}_{i1}, \mathbf{v}_{i2}, \ldots, \mathbf{v}_{i\wp}]$ is the individual swarm particle's position vector, velocity vector respectively where $i = 1, 2, \ldots, N_p$ denotes the swarm particle number. $\mathbf{P_i} := [\mathbf{P}_{i1}, \mathbf{P}_{i2}, \ldots, \mathbf{P}_{i\wp}]$ is each swarm particle's optimal position vector. $\mathbf{P_g} := [\mathbf{P}_{g1}, \mathbf{P}_{g2}, \ldots, \mathbf{P}_{g\wp}]$ is the swarm global optimum position vector considering all swarm particle's.

In the main loop of PSO, at each iteration $\mathbf{k}$, the position of each particle is updated by first computing an updated velocity vector in the $\wp$ space region considering previous results in $\wp$ search space such as velocity $\bigvee_{\mathbf{i}}^{\mathbf{k-1}}$ (inertia influence), best-known position $\mathbf{P}_{\mathbf{i}}^{\mathbf{k-1}}$ (cognitive influence), swarm best known global position $\mathbf{P}_{\mathbf{g}}^{\mathbf{k-1}}$(social influence) and PSO algorithm parameters $\mathbf{W_i}, \mathbf{C_c}, \mathbf{S_c}$:

$$\bigvee_{i}^{\mathbf{k}} = \mathbf{W_i} \times \bigvee_{i}^{\mathbf{k-1}} + \mathbf{C_c} \times (\mathbf{P}_{\mathbf{i}}^{\mathbf{k}} - \chi_{\mathbf{i}}^{\mathbf{k}}) + \mathbf{S_c} \times (\mathbf{P}_{\mathbf{g}}^{\mathbf{k}} - \chi_{\mathbf{i}}^{\mathbf{k}}) \tag{A.1}$$

$$\chi_{\mathbf{i}}^{\mathbf{k}} = \chi_{\mathbf{i}}^{\mathbf{k-1}} + \bigvee_{i}^{\mathbf{k}} \tag{A.2}$$

The local and global best particle positions are calculated by the following equations

$$\mathbf{P}_{\mathbf{i}}^{\mathbf{k}} = \begin{cases} \chi_{\mathbf{i}}^{\mathbf{k}} & \text{if } Y(\chi_{\mathbf{i}}^{\mathbf{k}}) < Y(\mathbf{P}_{\mathbf{i}}^{\mathbf{k-1}}) \\ \mathbf{P}_{\mathbf{i}}^{\mathbf{k-1}} & \text{otherwise} \end{cases} \tag{A.3}$$

$$\mathbf{P}_{\mathbf{g}}^{\mathbf{k}} = \begin{cases} \mathbf{P}_{\mathbf{i}}^{\mathbf{k}} & \text{if } Y(\mathbf{P}_{\mathbf{i}}^{\mathbf{k}}) < Y(\mathbf{P}_{\mathbf{g}}^{\mathbf{k-1}}) \\ \mathbf{P}_{\mathbf{g}}^{\mathbf{k-1}} & \text{otherwise} \end{cases} \tag{A.4}$$

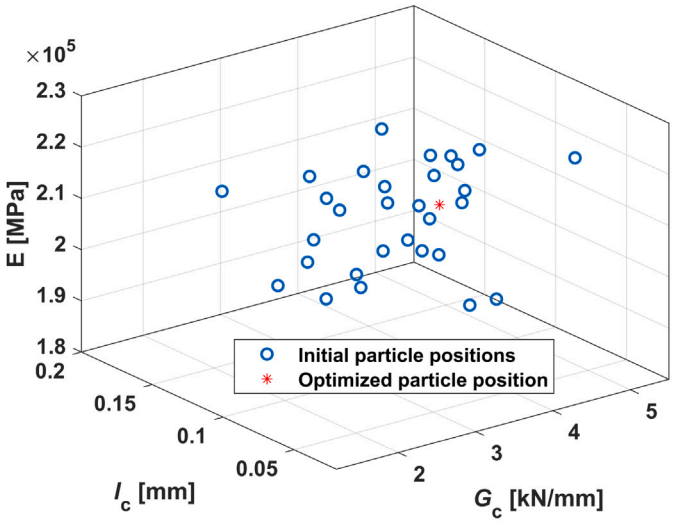

(a) Initial particles' position for PSO and TLBO algorithms

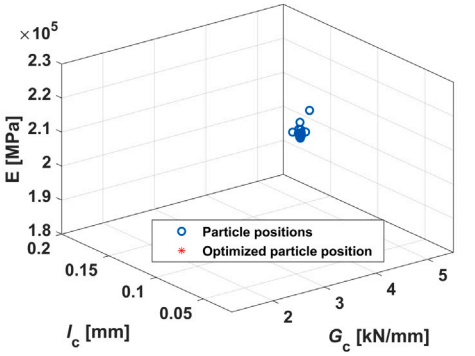

(b) final PSO converged particles solution

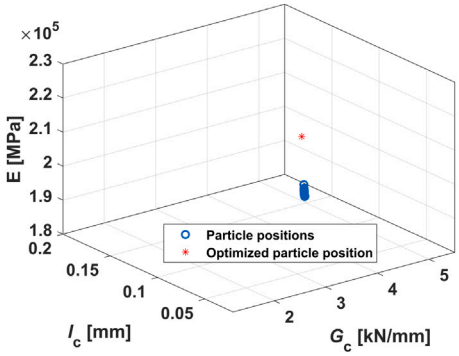

(c) final TLBO converged particles solution

Fig. 8. Comparison of performance of PSO and TLBO algorithms for parameters' identification.

(a) Photo of ABS dog-bone specimens

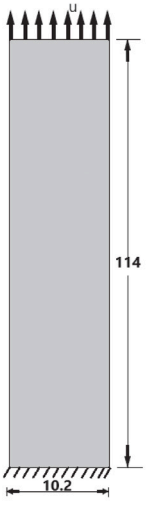

(b) Boundary conditions and geometrical data

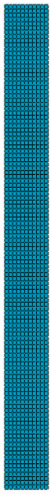

(c) FE mesh

Fig. 9. Photo of the specimen, dimensions and boundary conditions, FE mesh.

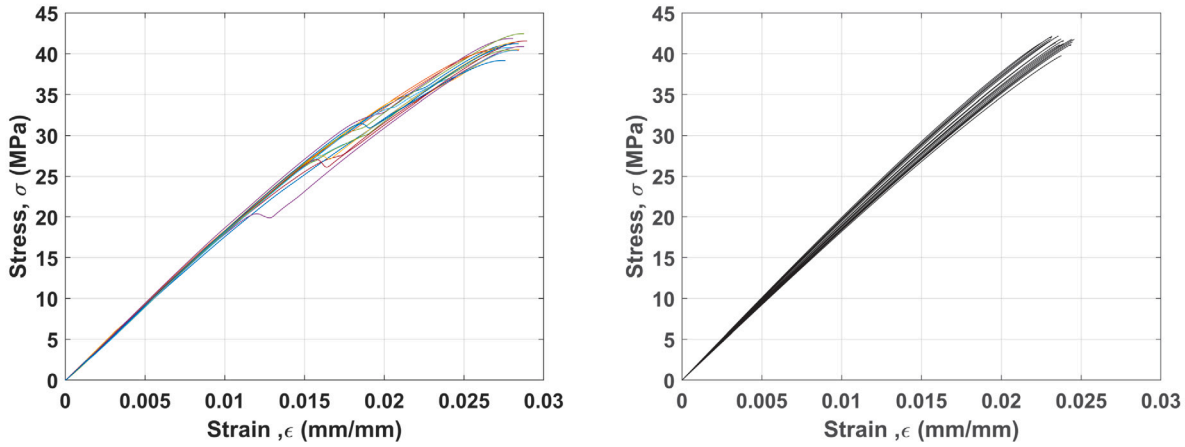

(a) Experimental results (b) Numerical simulations

Fig. 10. Experimental and numerical simulation results identified (corresponding to the identified model parameters).

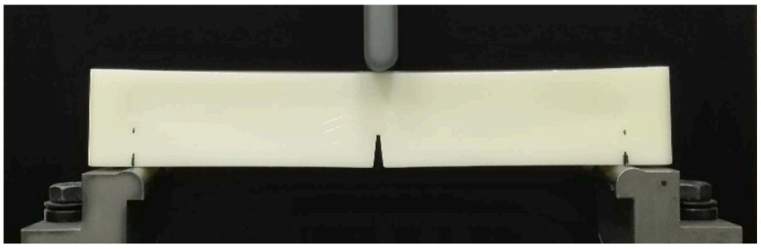

(a) Undeformed specimen

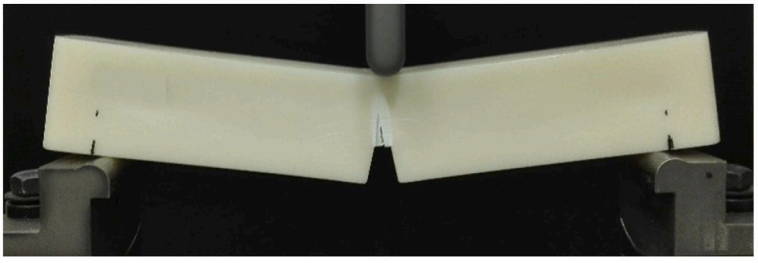

(b) Deformed specimen at failure

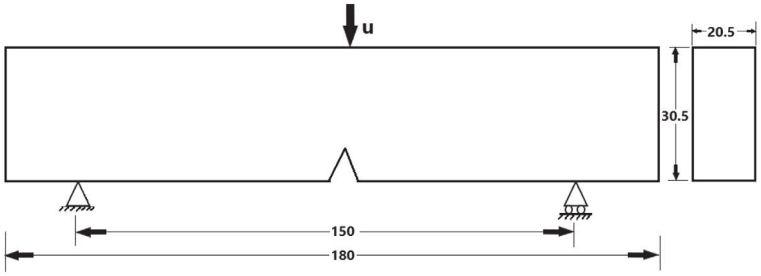

(c) Geometry and boundary conditions (measures in mm)

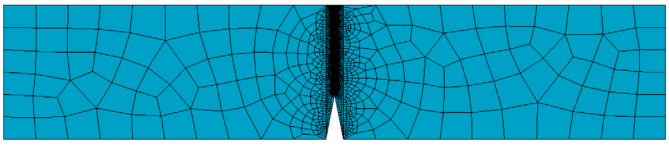

(d) FE model

Fig. 11. Experiment specimen and geometrical details (in mm), loading, boundary condition, meshing details of a numerical model for three-point bending loading case.

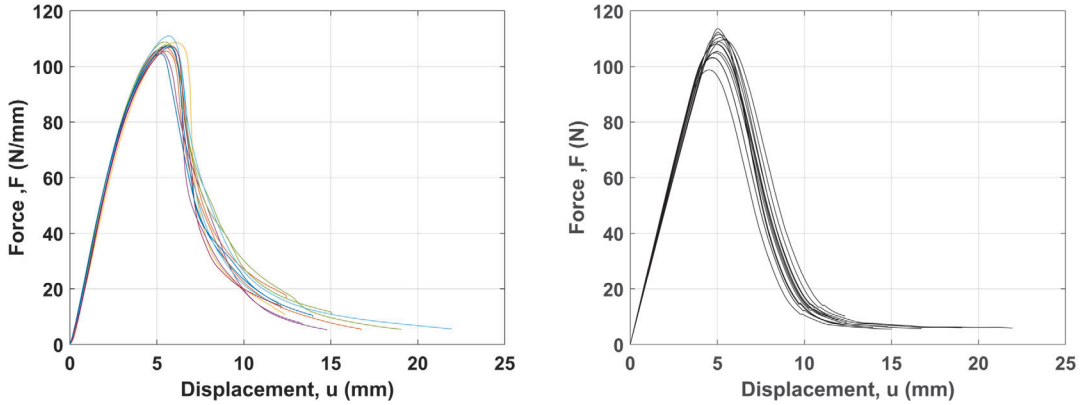

(a) Experimental results (b) Numerical simulation results

Fig. 12. Representation of experimental and numerical simulations of 15 force–displacement curve results.

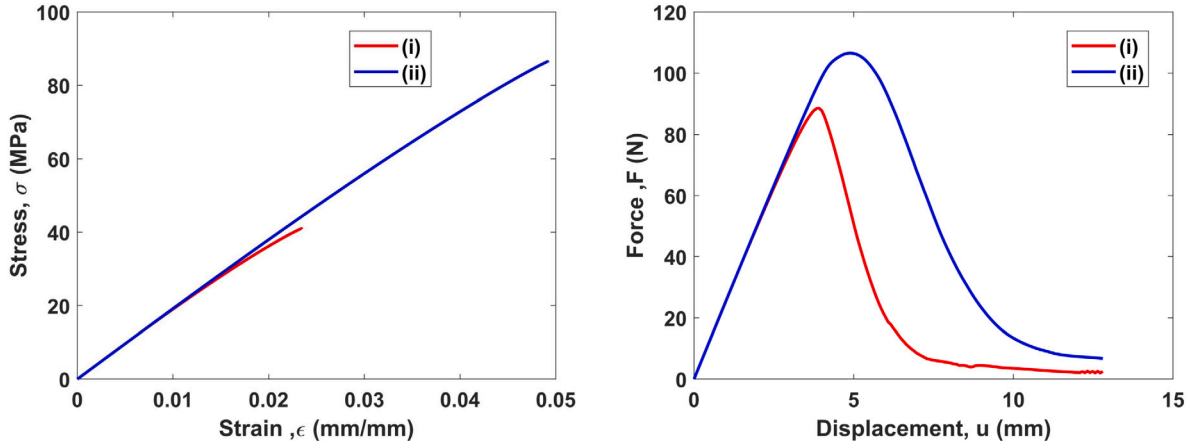

(a) Uni-axial tensile test (b) Three-point bending test

Fig. 13. Comparison between numerical results with parameters identified: (i) from uni-axial tensile tests (l_c = 1.37 mm, E = 1157.90 MPa, G_C = 7.5 N/mm); (ii) from notched three-point bending tests (l_c = 0.35 mm, E = 1153.07 MPa, G_C = 8.85 N/mm). The comparison highlights that it is necessary to identify the AT2 PF model parameters independently for each type of test.

References

[1] P. Wawrzynek, A.R. Ingraffea, Interactive finite element analysis of fracture processes: an integrated approach, Theor. Appl. Fract. Mech. 8 (1987) 137–150.

[2] M. Paggi, A. Carpinteri, On the stress singularities at multimaterial interfaces and related analogies with fluid dynamics and diffusion, Appl. Mech. Rev. 61 (2) (2008) 020801, http://dx.doi.org/10.1115/1.2885134.

[3] J. Lemaitre, R. Desmorat, Engineering Damage Mechanics: Ductile, Creep, Fatigue and Brittle Failures, Springer-Verlag, Berlin, 2005.

[4] Z. Bažant, T. Pijaudier-Cabot, Nonlocal continuum damage, localization instability and convergence, J. Appl. Mech. 55 (1988) 287–293.

[5] M. Jirásek, Nonlocal models for damage and fracture: Comparison of approaches, Int. J. Solids Struct. 35 (1998) 4133–4145.

[6] S. Forest, Micromorphic approach for gradient elasticity, viscoplasticity, and damage, J. Eng. Mech. 135 (2009) 117–131.

[7] B. Dimitrijevic, K. Hackl, A regularization framework for damage-plasticity models via gradient enhancement of the free energy, Int. J. Numer. Methods Biomed. Eng. 27 (2011) 1199–1210.

[8] R. Peerlings, M. Geers, R. de Borst, B. W., A critical comparison of non local and gradient-enhanced softening continua, Int. J. Solids Struct. 38 (2001) 7723—7746.

[9] N. Moës, J. Dolbow, T. Belytschko, A finite element method for crack growth without remeshing, Internat. J. Numer. Methods Engrg. 46 (1999) 131–150.

[10] J. Dolbow, N. Moës, T. Belytschko, An extended finite element method for modeling crack growth with contact, Comput. Methods Appl. Mech. Engrg. 190 (2001) 6825–6846.

[11] T. Fries, T. Belytschko, The extended/generalized finite element method: an overview of the method and its applications, Internat. J. Numer. Methods Engrg. 84 (2010) 253–304.

[12] J. Simo, J. Oliver, F. Armero, An analysis of strong discontinuities induced by strain-softening in rate-independent inelastic solids, Comput. Mech. 12 (1993) 277–296.

[13] C. Linder, F. Armero, Finite elements with embedded strong discontinuities for the modeling of failure in solids, Internat. J. Numer. Methods Engrg. 72 (2007) 1391–1433.

[14] F. Armero, C. Linder, New finite elements with embedded strong discontinuities for finite deformations, Comput. Methods Appl. Mech. Engrg. 198 (2008) 3138–3170.

[15] J. Oliver, A. Huespe, S. Blanco, D. Linero, Stability and robustness issues in numerical modeling of material failure with the strong discontinuity approach, Comput. Methods Appl. Mech. Engrg. 195 (2006) 7093–7114.

[16] G. Francfort, J.-J. Marigo, Revisiting brittle fracture as an energy minimization problem, J. Mech. Phys. Solids 46 (8) (1998) 1319–1342.

[17] L. Ambrosio, V. Tortorelli, Approximation of functional depending on jumps by elliptic functional via Γ-convergence, Comm. Pure Appl. Math. 43 (8) (1990) 999–1036.

[18] A. Griffith, The phenomena of rupture and flow in solids, Phil. Trans. R. Soc. Lond. Ser. A 221 (1921) 163–198.

[19] B. Bourdin, G.A. Francfort, J.-J. Marigo, Numerical experiments in revisited brittle fracture, J. Mech. Phys. Solids 48 (4) (2000) 797–826.

[20] C. Miehe, M. Hofacker, F. Welschinger, A phase field model for rate-independent crack propagation: Robust algorithmic implementation based on operator splits, Comput. Methods Appl. Mech. Engrg. 199 (45–48) (2010) 2765–2778.

[21] M. Ambati, T. Gerasimov, L. De Lorenzis, A review on phase-field models of brittle fracture and a new fast hybrid formulation, Comput. Mech. 55 (2015) 383–405.

[22] K.D. Nguyen, C.-L. Thanh, H. Nguyen-Xuan, M. Abdel-Wahab, A hybrid phase-field isogeometric analysis to crack propagation in porous functionally graded structures, Eng. Comput. (2021) 1–21.

[23] K.D. Nguyen, C.-L. Thanh, F. Vogel, H. Nguyen-Xuan, M. Abdel-Wahab, Crack propagation in quasi-brittle materials by fourth-order phase-field cohesive zone model, Theor. Appl. Fract. Mech. 118 (2022) 103236.
[24] K.D. Nguyen, C.E. Augarde, W.M. Coombs, H. Nguyen-Xuan, M. Abdel-Wahab, Non-conforming multipatches for NURBS-based finite element analysis of higher-order phase-field models for brittle fracture, Eng. Fract. Mech. 235 (2020) 107133.
[25] R. Cavuoto, P. Lenarda, D. Misseroni, M. Paggi, D. Bigoni, Failure through crack propagation in components with holes and notches: An experimental assessment of the phase field model, Int. J. Solids Struct. 257 (2022) 111798.
[26] L. Ambrosio, On the approximation of free discontinuity problems, Boll. Union. Mat. Ital., B (7) (1992) 105–123.
[27] S. Burke, C. Ortner, E. Süli, An adaptive finite element approximation of a generalized Ambrosio–Tortorelli functional, Math. Models Methods Appl. Sci. 23 (09) (2013) 1663–1697.
[28] E. Tanné, T. Li, B. Bourdin, J.-J. Marigo, C. Maurini, Crack nucleation in variational phase-field models of brittle fracture, J. Mech. Phys. Solids 110 (2018) 80–99.
[29] T. Wu, B. Rosić, L. De Lorenzis, H.G. Matthies, Parameter identification for phase-field modeling of fracture: a Bayesian approach with sampling-free update, Comput. Mech. 67 (2021) 435–453.
[30] V. Carollo, D. Piga, C. Borri, M. Paggi, Identification of elasto-plastic and nonlinear fracture mechanics parameters of silver-plated copper busbars for photovoltaics, Eng. Fract. Mech. 205 (2019) 439–454.
[31] C. Miehe, M. Lambrecht, Algorithms for computation of stresses and elasticity moduli in terms of Seth–Hill's family of generalized strain tensors, Commun. Numer. Methods. Eng. 17 (5) (2001) 337–353.
[32] B. Bourdin, G.A. Francfort, J.-J. Marigo, The variational approach to fracture, J. Elasticity 91 (2008) 5–148.
[33] T.J. Hughes, J.A. Cottrell, Y. Bazilevs, Isogeometric analysis: CAD, finite elements, NURBS, exact geometry and mesh refinement, Comput. Methods Appl. Mech. Engrg. 194 (39–41) (2005) 4135–4195.
[34] D. Whitley, A genetic algorithm tutorial, Stat. Comput. 4 (1994) 65–85.
[35] J. Kennedy, R. Eberhart, Particle swarm optimization, in: Proceedings of ICNN'95-International Conference on Neural Networks, Vol. 4, IEEE, 1995, pp. 1942–1948.
[36] R.V. Rao, V.J. Savsani, D. Vakharia, Teaching–learning-based optimization: a novel method for constrained mechanical design optimization problems, Comput. Aided Des. 43 (3) (2011) 303–315.
[37] R. Rao, Jaya: A simple and new optimization algorithm for solving constrained and unconstrained optimization problems, Int. J. Ind. Eng. Comput. 7 (1) (2016) 19–34.
[38] M. Clerc, The swarm and the queen: towards a deterministic and adaptive particle swarm optimization, in: Proceedings of the 1999 Congress on Evolutionary Computation-CEC99 (Cat. No. 99TH8406), Vol. 3, IEEE, 1999, pp. 1951–1957.
[39] R.C. Eberhart, Y. Shi, Comparing inertia weights and constriction factors in particle swarm optimization, in: Proceedings of the 2000 Congress on Evolutionary Computation. CEC00 (Cat. No. 00TH8512), Vol. 1, IEEE, 2000, pp. 84–88.
[40] A.R. Torrado, C.M. Shemelya, J.D. English, Y. Lin, R.B. Wicker, D.A. Roberson, Characterizing the effect of additives to ABS on the mechanical property anisotropy of specimens fabricated by material extrusion 3D printing, Addit. Manuf. 6 (2015) 16–29.
[41] J.-Y. Wu, A unified phase-field theory for the mechanics of damage and quasi-brittle failure, J. Mech. Phys. Solids 103 (2017) 72–99.
[42] K. Pham, H. Amor, J.-J. Marigo, C. Maurini, Gradient damage models and their use to approximate brittle fracture, Int. J. Damage Mech. 20 (4) (2011) 618–652.
[43] T.K. Mandal, V.P. Nguyen, J.-Y. Wu, Length scale and mesh bias sensitivity of phase-field models for brittle and cohesive fracture, Eng. Fract. Mech. 217 (2019) 106532.